Supplement of Geosci. Model Dev., 18, 6439–6460, 2025
https://doi.org/10.5194/gmd-18-6439-2025-supplement

Geoscientific Model Development
Open Access
EGU

Supplement of

High-resolution mapping of urban NO_2 concentrations using Retina v2: a case study on data assimilation of surface and satellite observations in Madrid

Bas Mijling et al.

Correspondence to: Bas Mijling (bas.mijling@knmi.nl)

Table of Contents

S1 Validation of background concentrations

The approach for calculation of the background concentration, described in Section 2.2.1, is motivated by the need for a straightforward method using the coarse-resolution data from the CAMS regional ensemble, while avoiding double counting of NO_2 from local emission sources. Validation of this method is presented in the Figure S1.

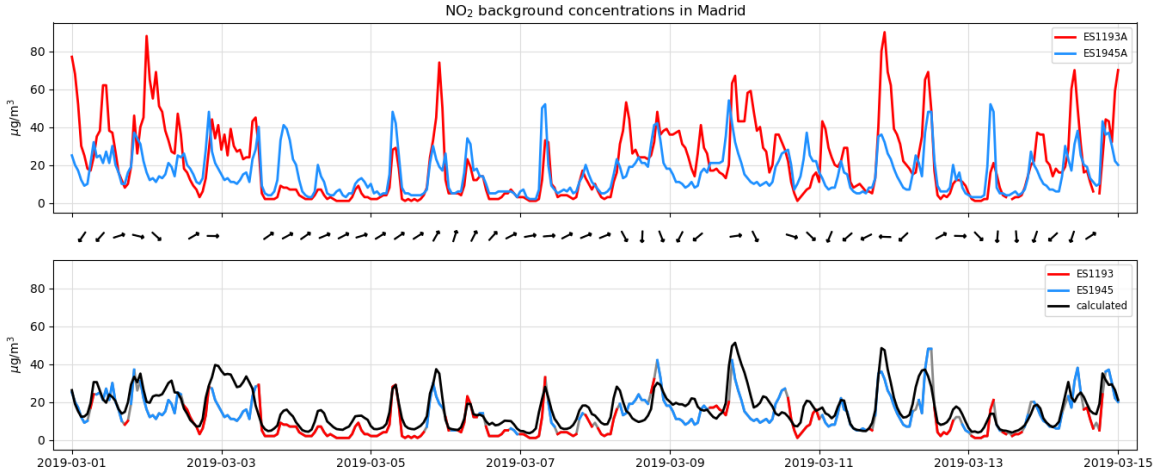

Figure S1: Hourly NO_2 concentrations measured at two suburban background locations, and the comparison against background concentrations calculated from the NO_2 concentration fields from the CAMS regional ensemble.

The top panel shows NO_2 measurements from two suburban background stations: ES1193 (Casa de Campo) and ES1945 (El Pardo), which consistently record the lowest concentrations in the area. A third station, ES1946, also classified as suburban background, is excluded due to its elevated readings, likely influenced by nearby urbanization and proximity to Barajas International Airport. The time series show that the lowest NO_2 concentrations alternate between the two selected stations. This variation is partly explained by wind direction, represented by black arrows indicating 6-hour intervals. Typically, El Pardo registers lower NO_2 levels when clean air arrives from the northeast to northwest, whereas Casa de Campo, being downwind, includes additional local pollution contributions.

The bottom panel compares the lowest NO_2 concentration measured between the two stations with the background concentration calculated from CAMS data along the partial municipal perimeter, as described in Section 2.2.1. The close agreement between the calculated background and the observed minima suggests that this method provides a realistic estimate of background NO_2 under varying meteorological conditions.

S2 Estimating the NO_2/NOx ratio at the surface

In the previous Retina version (Mijling 2020) we implemented the Ozone Limiting Method (OLM) as described in EPA (2015). The method uses ambient ozone (O_3) to determine which fraction of NO is converted to NO_2. O_3 concentrations are taken from the CAMS regional ensemble. The dispersed (locally produced) NOx concentration is divided into two components: the primary emitted NO_2 (here assumed to be 10%) and the remaining NOx, which is assumed to be all NO available for reaction with ambient O_3: $NO + O_3 \rightarrow NO_2 + O_2$

If the mixing ratio of ozone (O_3) is larger than the 90% of NOx, then all NO is converted to NO_2. Otherwise, the amount of NO converted is equal to the available O_3, i.e. $(NO_2) = 0.1(NOx) + (O_3)$. The reaction is assumed to be instantaneous and irreversible. The resulting NO_2 concentration is added to the NO_2 background concentration. The OLM is a clear oversimplification as it assumes an instantaneous conversion from NO to NO_2 and neglects the photochemistry from NO_2 back to NO.

Figure S1 shows diurnal cycles of NO_2 ratios based on measurements of NO and NO_2 at a roadside station for two different months. In wintertime, the NO_2 ratio drops to lower values when the morning rush hour starts. The low temperatures slow down a fast conversion of primary emitted NO (mainly from nearby tail pipes) to NO_2.

This conversion is faster in summer, resulting in higher NO_2 ratios during the day. During the night, when no significant photolysis takes place, NO_2 ratios are high in both seasons.

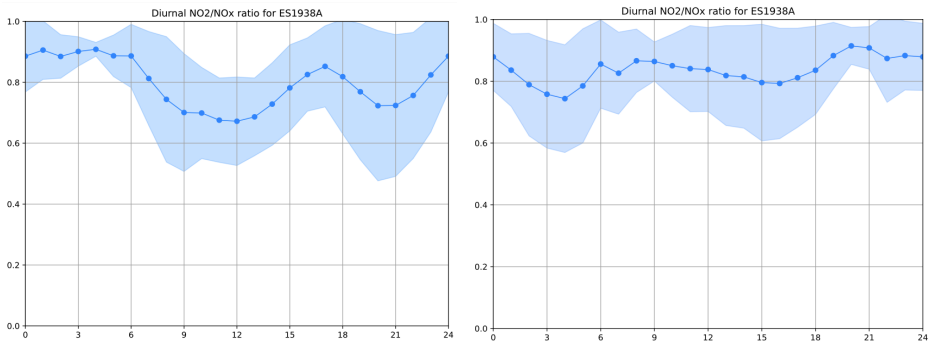

Figure S2: Averaged diurnal NO_2 ratios from hourly observations of NO and NO_2 at Castellana road station, for January 2022 (left) and July 2022 (right). The shaded area indicates the standard deviation.

We want to estimate the NO_2 ratio from parameters (*features*) which are available at simulation time:

- local NOx concentration, i.e. the quantity which is simulated by the dispersion model (excluding the background concentration).
- background O_3 concentration, taken from the regional CAMS ensemble.
- background NO_2 concentration, taken from the regional CAMS ensemble.
- temperature, as a measure of reaction speed for conversion NO to NO_2.
- solar elevation angle (SEA), as a measure of radiation available for photolysis of NO_2.

We use a training data set consisting of 810,071 records, spanning a 5-year period (2018-2022), taken from the 14 reference stations in Madrid which simultaneously measure NO_2, NO and O_3. The corresponding solar elevation angles are calculated from latitude, longitude, the time in UTC, and the day of the year.

As the relation between the NO_2 ratio and these parameters is likely to be non-linear, we prefer machine learning methods above multiple linear regression. We opt for XGBoost for its rapid learning time and superior accuracy compared Random Forest. Additionally, the trained XGBoost model has a more compact file size when stored for future use. Being a tree-based model, it allows us to calculate the importance of each feature. From Fig. S2 can be seen that all selected features contribute significantly to the prediction of the NO_2 ratio.

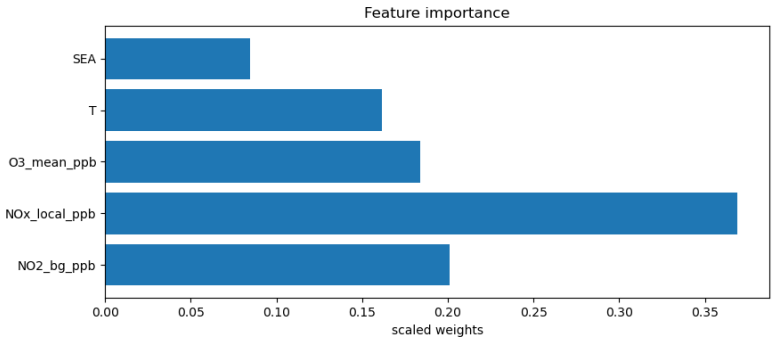

Figure S3: Feature importance in predicting the NO_2 ratio, represented as scaled weights.

The improvement of the XGBoost model over OLM is shown in Fig. S3. Here both methods are used to predict NO_2 concentrations for a given NO_2 and O_3 background (taken from CAMS) and a locally produced NOx concentration. Especially for street stations the OLM introduces positive biases, related to the assumption of instantaneous NO to NO_2 conversion. The portability of the Madrid-trained model is shown in the bottom right panel where it is applied to observations of a street station in Amsterdam, resulting in good correspondence with observations.

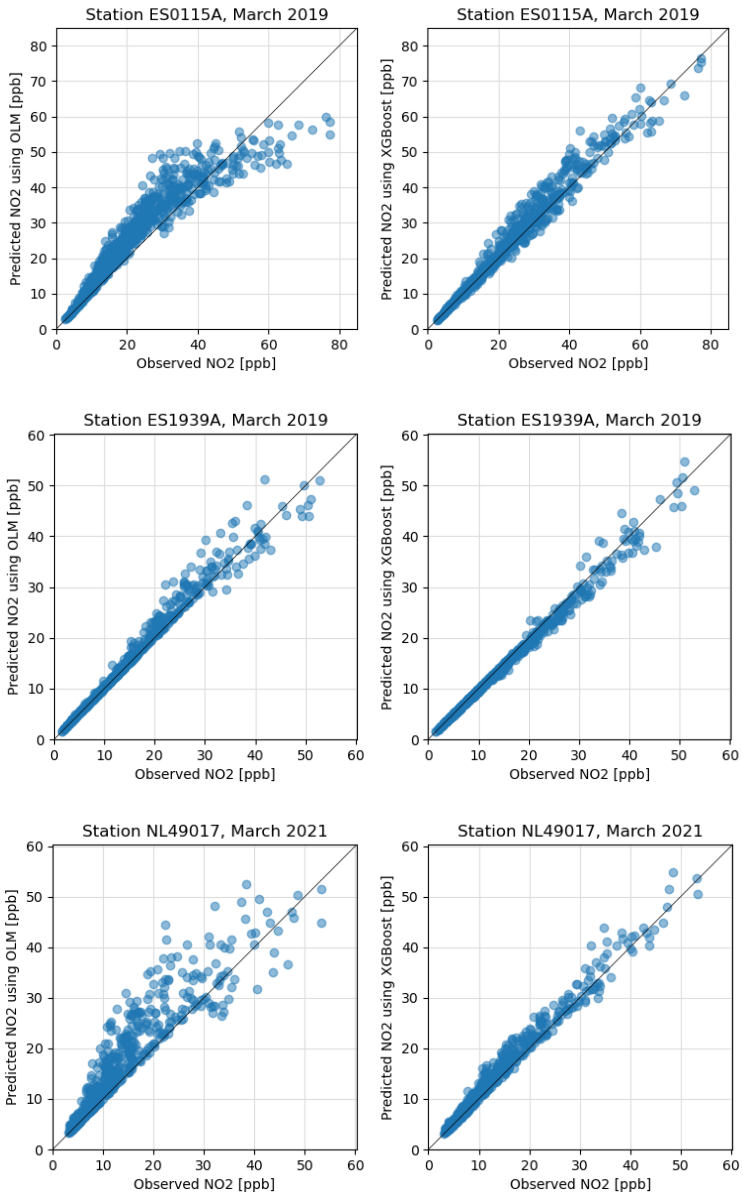

Figure S4: Comparison of predicted NO_2 concentrations (based on locally produced NOx, and NO_2 and O_3 background concentrations) against observed NO_2 concentrations. Left panels show results for the OLM, right panels show results for the XGBoost model. Observations are taken from a street station (ES0115A) and an urban background station (ES1939A) in Madrid, and a street station in Amsterdam (NL49017).

S3 Estimating the NO_2/NOx ratio in tropospheric columns

Figure S4 shows the daily NO_2/NOx ratio at 13 UTC for 4 cities as found in simulations by the CAMS regional ensemble for 2019. Note that NO_2/NOx ratios in columns are generally higher than surface ratios due to increased ozone availability. There is a seasonal cycle visible which has a maximum in summertime for Barcelona and Madrid, but a maximum in wintertime for Amsterdam and Oslo. There are competing processes at work, roughly between temperature (formation of NO_2 from NO) and sunlight (photodissociation of NO_2 to NO).

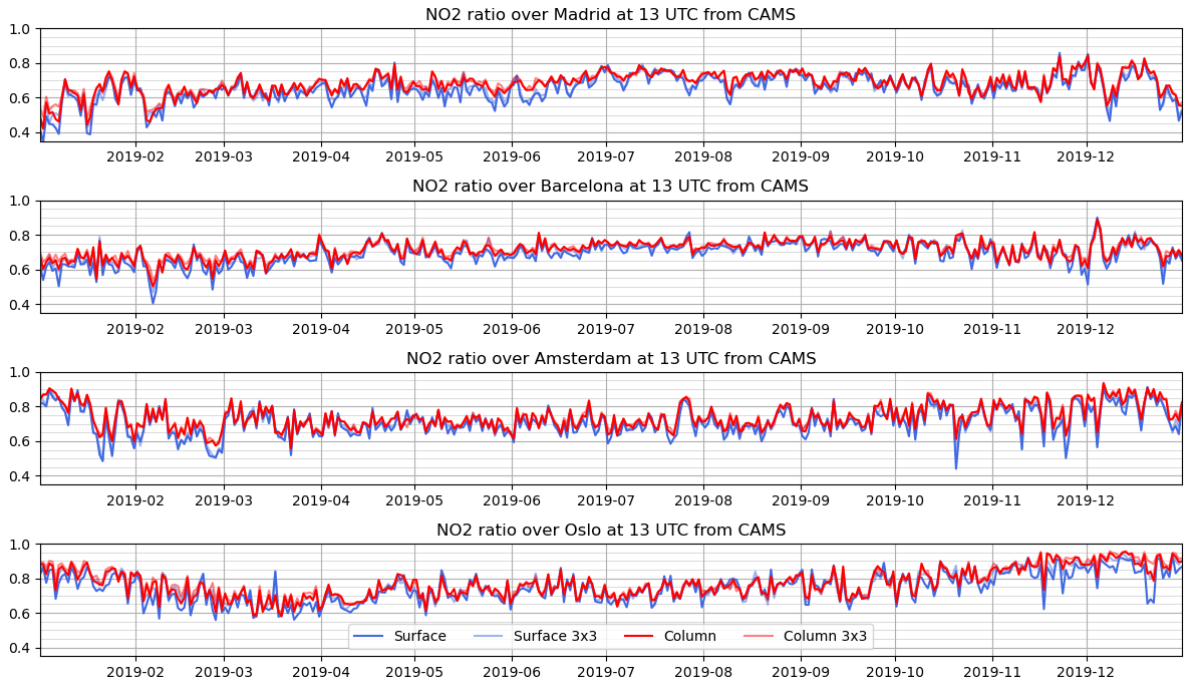

Figure S5: Daily NO_2/NOx ratio at 13 UTC for 4 cities as found in simulations by the CAMS regional ensemble for 2019. In blue: NO_2 surface ratio for centre grid cell, and average surface ratio for the larger 3x3 grid cell area. In red: NO_2 column ratio for centre grid cell, and average column ratio for 3x3 grid cell.

S4 Estimating emission factors from observations

We want to estimate the emission factors x_j such that the concentration simulations (either surface or column concentrations) y_i best match the observations. Writing Eq. 6 as

$$y_i = b_i + r_i \sum_j \alpha_{ij} x_j \tag{S1}$$

we can see that it can be interpreted as a matrix equation from which x_j must be solved. For n ground stations, we have $24n$ hourly in-situ measurements in a 24-hour period. For the Madrid area, there are about 14 column retrievals in this period (in general this number will depend on the domain size and cloud cover).

We stabilise the estimation of the emission factors using a Kalman filter. Let vector $\mathbf{x}$ consist of 25 elements: one emission factor for traffic, and 24 elements describing the diurnal cycle of the residential emissions. Starting from *a priori* values at $t = 0$, the 24-h update (analysis) of the state vector depends on the difference between the observation vector $\mathbf{y}_{\mathrm{obs}}$ and the simulation vector $\mathbf{y}_{\mathrm{sim}}$:

$$\mathbf{x}_t = \mathbf{x}_{t-1} + \mathbf{K}(\mathbf{y}_{\mathrm{obs}} - \mathbf{y}_{\mathrm{sim}}) \tag{S2}$$

Note that $\mathbf{y}$ can contain both in-situ surface concentrations as column concentrations of NO_2. $\mathbf{K}$ is the Kalman gain matrix, calculated from

$$\mathbf{K} = \mathbf{P}^{\mathrm{f}}\mathbf{H}^{\mathrm{T}}\left(\mathbf{H}\mathbf{P}^{\mathrm{f}}\mathbf{H}^{\mathrm{T}} + \mathbf{R}\right)^{-1} \tag{S3}$$

in which $\mathbf{R}$ is the observation error covariance matrix. This is a diagonal matrix (the air pollution measurements are uncorrelated) with the observational variances on the diagonal. $\mathbf{P}^{\mathrm{f}}$ is the error covariance matrix of the forecast, i.e. the expected error covariance in the state vector elements. The errors are converted from state space to observational space by $\mathbf{H}$, the Jacobian of the observation operator. Element H_{ij} of this matrix represents the partial derivative of observation y_i to state vector element x_j. Neglecting non-linearity due to ozone interference, these elements can be written as

$$H_{ij} = r_i \alpha_{ij} \tag{S4}$$

Kalman filtering reduces the error covariance of the state vector elements, leading to the error covariance analysis calculated by

$$\mathbf{P}^{\mathrm{a}} = (\mathbf{I} - \mathbf{KH})\mathbf{P}^{\mathrm{f}} \tag{S5}$$

This analysis is accumulated with matrix $\mathbf{Q}$ in the next step of the filter, reflecting the increase in uncertainty of the emission factors in the 24-h period between the evaluation moments:

$$\mathbf{P}_t^{\mathrm{f}} = \mathbf{P}_{t-1}^{\mathrm{a}} + \mathbf{Q} \tag{S6}$$

Matrix $\mathbf{Q}$ can be used to tune the Kalman filtering. For small $\mathbf{Q}$ the emission factor update will be relatively insensitive to the observations, resulting in longer response (lag) times. For larger $\mathbf{Q}$ the response time will be faster, but this comes at the expense of increased noise. We decompose $\mathbf{Q}$ as

$$\mathbf{Q} = \mathrm{diag}(\boldsymbol{\sigma})\ \mathbf{C}\ \mathrm{diag}(\boldsymbol{\sigma})\ , \tag{S7}$$

in which $\mathbf{C}$ is the correlation matrix, describing the coupling between the state vector elements, and $\boldsymbol{\sigma}$ represents a vector of added errors. $\boldsymbol{\sigma}$ is taken as relative errors from the state vector elements

$$\sigma_1 = \varepsilon x_1 \tag{S8}$$

$$\sigma_i = \varepsilon \overline{x_{\mathrm{res}}}\ ,\ \text{for } i = 2,\ldots,25$$

$\overline{x_{\mathrm{res}}}$ is the average of the residential emission factors, calculated as

$$\overline{x_{\mathrm{res}}} = \frac{1}{24}\sum_{h=1}^{24} x_{h+1} \tag{S9}$$

We take $\varepsilon = 0.03$ as practical value.

When no hourly surface measurements are present (i.e. only space observations), the satellite measurements can only sample the diurnal cycle at overpass time. We couple all elements of the residential diurnal cycle $(x_2, \ldots, x_{25})$ un matrix $\mathbf{C}$ as follows:

$$C_{ij} = \begin{cases} 0\ , & \text{for } (i \geq 2, j = 1) \text{ and } (i = 1, j \geq 2) \\ 1\ , & \text{elsewhere} \end{cases} \tag{S10}$$

such that not only the element at overpass time will be updated, but that the entire residential profile will be scaled.

When hourly surface measurements are present, we choose the off-diagonal elements for the residential cycle in $\mathbf{C}$ to correlate depending on their lag h_{ij} in hours:

$$C_{ij} = \begin{cases} 1 & , \text{for } i = j \\ 0 & , \text{for } (i \geq 2, j = 1) \text{ and } (i = 1, j \geq 2) \\ (1 + ph_{ij})\exp(-ph_{ij}) & , \text{elsewhere} \end{cases} \tag{S11}$$

For instance, the time lag between x_2 and x_3 is 1 hour, as is the time lag between x_2 and x_{25}. The Thiebaux autoregressive correlation function is less steep at larger distances than the (often chosen) Gaussian function, improving the condition number of matrix $\mathbf{P}^{\mathrm{f}}$ while maintaining the coupling between neighbouring elements. By setting parameter $p = 0.6$ in the Thiebaux function the correlation drops from 1 to 0.5 for a lag of ~2.8 h.

S4.1 Collinearity

The algorithm is not always capable of resolving the individual sectoral contributions from NO_2 observations, particularly when using satellite data due to its coarse spatial resolution. This collinearity can result in unrealistic solutions, with excessive emissions being attributed either to the transport sector or the residential sector. We force a better balancing between the emission sectors by adding a larger error to the sector which contributes less to the total emissions. This is established by redefining Eq. (S8) as

$$\sigma_1 = \varepsilon\left(x_1 + \frac{P_{\mathrm{res}}}{P_{\mathrm{tra}}}\overline{x_{\mathrm{res}}}\right) \tag{S12}$$

$$\sigma_i = \varepsilon \left(\frac{P_{\text{tra}}}{P_{\text{res}}} x_1 + \overline{x_{\text{res}}} \right) \text{ , for } i = 2, \ldots, 24$$

In which P_{tra} is the sum of proxy emissions of the transport sector in the domain, and P_{res} is the sum of proxy emissions for the residence sector in the domain.

S4.2 Negative values

Given their physical meaning, only positive values for the state vector elements are allowed. However, the Kalman filtering in Eq. (S2) can result in negative values in the analysis. When this occurs, the covariance matrix $\mathbf{P}^{\text{f}}$ is decomposed as in Eq. (S7). The standard deviations σ_i for elements that became negative are halved (the smaller error will make it more difficult for the state vector element to drop below zero). A new $\mathbf{P}^{\text{f}}$ is reconstructed based on the adjusted $\boldsymbol{\sigma}$ and the Kalman filter is then reapplied. This process is repeated until all elements are positive after filtering, with a maximum of 20 iterations before giving up.

S5 Diurnal cycles in residential emissions

Since population density is used as a proxy for residential emissions, we lack information on the diurnal cycle of these emissions. This can be estimated from hourly measurements, as explained above. However, if we use TROPOMI observations only, we can only infer emission estimates around overpass time. In that case, we rely on a well-chosen a priori profile.

A good candidate would be the hourly temporal profile for the residential sector provided by the CAMS-TEMPO dataset (Guevara et al., 2020). This profile presents two peaks, one in the morning and one in the afternoon, when energy consumption is supposedly higher due to increased space heating or cooking activities (see Fig. S5). However, using this profile in the Retina algorithm introduces unwanted biases, particularly in the early morning and late evening. Better results are achieved with an averaged profile generated by the algorithm itself from a emission optimisation run over 2019 using data of 20 reference stations in Madrid. This profile features a distinct peak around 10:00. It should be noted that this profile does not necessarily represent a more realistic cycle for the residential sector, as it also compensates systematic hourly biases in the algorithm, such as incorrectly assumed traffic emission cycles or incomplete NOx chemistry.

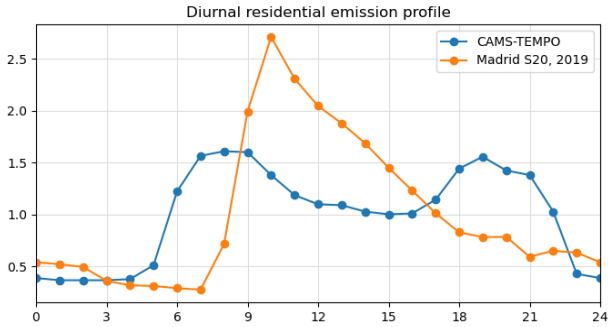

Figure S6: Comparison of diurnal temporal profiles for the residential sector from CAMS-TEMPO (blue line) and Retina (orange line), generated using measurements from 20 reference stations in Madrid during 2019. Both profiles are normalized to 1.

S6 Spatial assimilation: model error covariance

For optimal interpolation a realistic representation of the model error covariance is essential, as it strongly determines the behaviour of the optimal interpolation. The covariance between two locations $\mathbf{x}_1$ and $\mathbf{x}_2$ for a given hour t is defined as

$$\text{cov}(\mathbf{x}_1, \mathbf{x}_2, t) = \sigma_1(t) \rho(\mathbf{x}_1, \mathbf{x}_2, t) \sigma_2(t) \text{ ,} \tag{S13}$$

where σ_1 and σ_2 are the model errors at the corresponding locations. ρ represents the correlation between the errors at time t. A classical approach for modelling ρ is by assuming a Gaussian decay over distance $d = \|\mathbf{x}_1 - \mathbf{x}_2\|$, parameterized by correlation length L:

$$\rho(d) = \exp(-(d/L)^2) \tag{S14}$$

Note that this approach is time-independent and isotropic. We refine the covariance modelling by including spatial representativity of the observations (which is different for street locations than for background locations), and atmospheric dispersion (which changes every hour), writing:

$$\mathrm{cov}(\mathbf{x}_1, \mathbf{x}_2, t) = \sigma_1(t)\rho_A(\mathbf{x}_1, \mathbf{x}_2)\rho_B(\mathbf{x}_1 - \mathbf{x}_2, t)\sigma_2(t)\,, \tag{S15}$$

ρ_A represents the correlation between simulated time series at different locations. This time-independent correlation is precalculated for a given period between m locations where measurements are available and all other receptor locations, resulting in m correlation fields. As can be seen from Fig. S6, street locations correlate better with each other than background locations, and vice versa.

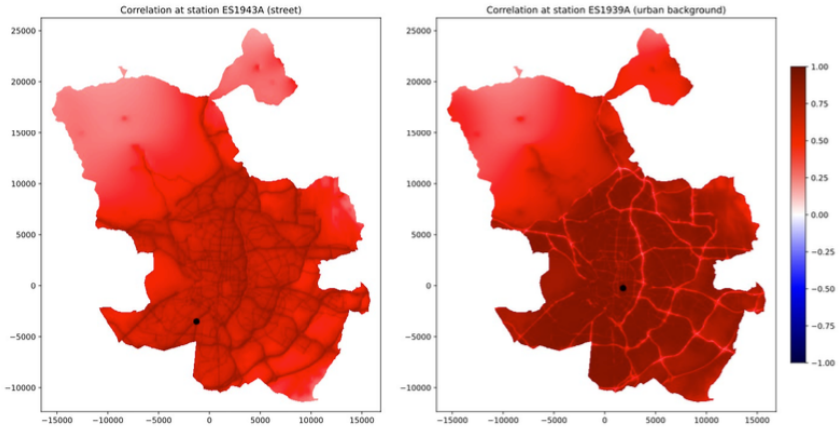

Figure S7: Examples of spatial correlation fields for a street location (left) and an urban background location (right). The locations are indicated with black dots.

ρ_B represents the correlation resulting from atmospheric dispersion. This dispersion determines the extent to which errors in simulated concentrations, caused by wrongly assumed emissions, can propagate to neighbouring areas. We want to express this correlation in terms of the dispersion kernel (i.e. the dispersion of a unit of emission calculated by AERMOD), as this information is available from previous calculations by Retina. Different kernels introduce different spatial correlation, depending e.g. on wind direction and atmospheric stability.

Assume a random signal $s_i(t)$, representing the unbiased error in emissions at location i. Assume a 1D kernel $k(x)$, describing how a unit of emission is dispersed as concentrations in downwind direction. This kernel is applied to random, uncorrelated signals $s_i(t)$ at equidistant locations, separated by distance Δ (see Fig. S7):

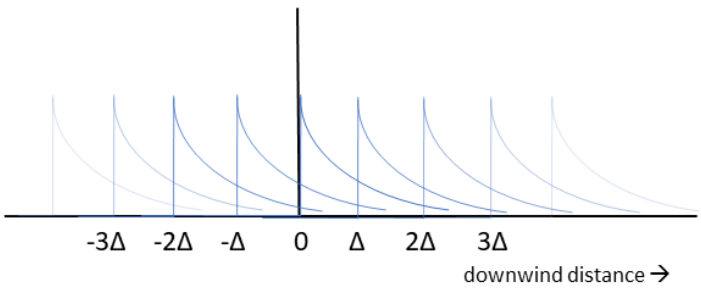

Figure S8: Schematic representation of the dispersion per unit emissions at equidistant locations along the downwind axis.

At origin, we have a superposition of concentrations from all signals transported by k:

$$c(0,t) = \sum_{i=-\infty}^{\infty} k(-i\Delta)s_i(t) \tag{S16}$$

At arbitrary distance x, the accumulated concentration is:

$$c(x,t) = \sum_{i=-\infty}^{\infty} k(-i\Delta + x)s_i(t) \tag{S17}$$

When signal $s_i(t)$ is written as a discrete signal s_{it} with $t = 1,\dots,T$ the covariance between two signals at two locations i and j can then be expressed as:

$$\mathrm{cov}(s_{it}, s_{jt}) \stackrel{\mathrm{def}}{=} \frac{1}{T}\sum_{t=1}^{T}(s_{it} - \overline{s_{it}})(s_{jt} - \overline{s_{jt}}) = \frac{1}{T}\sum_{t=1}^{T} s_{it}s_{jt} = \begin{cases} 0 & \text{for } i \neq j \\ 1 & \text{for } i = j \end{cases} \tag{S18}$$

The covariance between the concentrations found at locations 0 and x can now be calculated using Eqs. (S16)−(S18):

$$\begin{aligned} \mathrm{cov}\big(c(0,t), c(x,t)\big) &= \frac{1}{T}\sum_t \Big(\sum_i k(-i\Delta)s_{it}\Big)\Big(\sum_j k(-j\Delta + x)s_{jt}\Big) \\ &= \sum_i \sum_j k(-i\Delta)k(-j\Delta + x)\Big(\frac{1}{T}\sum_t s_{it}s_{jt}\Big) \\ &= \sum_{i=-\infty}^{\infty} k(-i\Delta)k(-i\Delta + x) \end{aligned} \tag{S19}$$

This can be interpreted as an element-wise multiplication of the kernel k with a copy of itself, shifted by distance x. In Retina, the 2D dispersion kernels from AERMOD are gridded on a regular high-resolution grid. $\rho_B(\mathbf{x}_1 - \mathbf{x}_2, t)$ in Eq. (S15) can therefore be calculated from an element-wise multiplication of the AERMOD kernel at time t with a copy of itself, shifted by a vector $\mathbf{d} = \mathbf{x}_1 - \mathbf{x}_2$. We use the covariance found for $\mathbf{d} = 0$ for scaling, such that $\rho_B(0) = 1$.

Figure S8 shows some examples of dispersion kernel correlations. Note the point symmetry in ρ_B, as $\rho_B(\mathbf{d}) = \rho_B(-\mathbf{d})$. The figure also clearly shows the symmetry axes along the downwind and crosswind direction. To speed up calculations of ρ_B, we calculate the dispersion kernel correlation field for a given time t once, and evaluate transects along the main axes. We fit range parameters L along each symmetry axis with a heuristically determined fit model

$$\rho(d) \approx \left(1 + \left|\frac{d}{L}\right|^{0.75}\right) exp\left(-\left|\frac{d}{L}\right|^{0.75}\right) \tag{S20}$$

This equation is a modification of the Thiebeaux function, which is found to be the best concession between providing high correlations at short distances, and a good description of the tails at longer distances.

L can be considered as the correlation length along a main axis. Once L_{dw} (along the downwind axis) and L_{cw} (along the crosswind axis) are determined, ρ_B can be calculated quickly for each $(\mathbf{x}_1, \mathbf{x}_2)$ using Eq. (S20) and assuming elliptical symmetry of the dispersion correlation field.

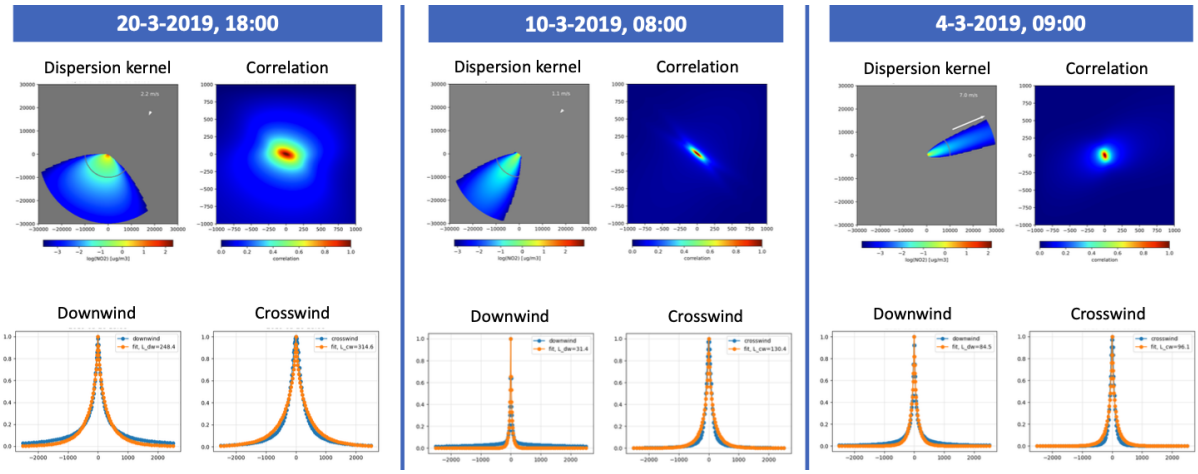

Figure S9: Three examples of correlation associated with different dispersion kernels in Madrid. Distances are in metres. The two symmetry axes are in downwind and crosswind direction. Transects along these axes are shown (blue lines), together with the numerical fit (orange lines).

S6 Simulation comparison TROPOMI and in-situ

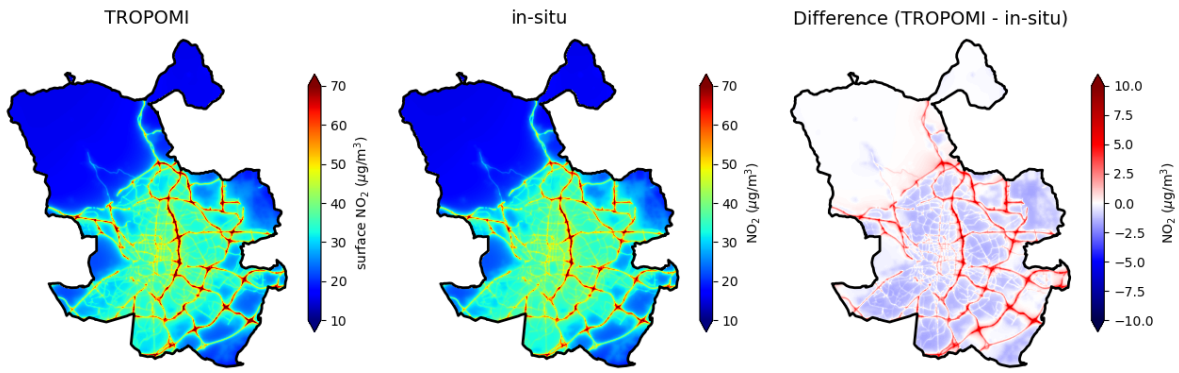

Figure S10: Comparison of simulation of surface concentrations for March 2019 in Madrid. (left) Simulation based on emission optimisation using TROPOMI data only. (center) Simulation based on emissions optimisation using in-situ measurements of 24 stations. The difference map (right) shows that the TROPOMI-based simulation results in up to 5 µg/m³ higher concentrations on roads and up to 1.5 µg/m³ lower concentrations in urban backgrounds.

S7 Seasonal performance of the Retina algorithm

To get a better insight in the seasonal behaviour of the Retina algorithm, we performed a processing for 2019 for three different scenarios:

(A) Emission optimisation based on TROPOMI only
(B) Emission optimisation based on 24 surface stations only
(C) Emission optimisation and spatial assimilation of 24 surface stations

Table S1 shows the validation statistics per month, based on time series of hourly simulation, averaged over the 24 stations. March 2019, indicated in bold font and evaluated in the main text, offers a reasonable approximation for the yearly performance.

Table S1: Monthly city-wide validation statistics for 2019

2019	Obs. (µg/m³)	Correlation			RMSE (µg/m³)			Bias (µg/m³)		
		A	B	C	A	B	C	A	B	C
January	55.6	0.760	0.788	0.908	23.7	22.2	16.3	-4.7	-0.5	-1.5
February	55.4	0.790	0.835	0.909	22.2	19.6	15.9	-4.9	-1.2	-1.6
March	**36.2**	**0.753**	**0.792**	**0.900**	**18.5**	**17.2**	**13.0**	**-2.7**	**1.1**	**-0.9**
April	27.3	0.728	0.752	0.892	15.0	14.6	11.0	-2.4	0.6	-0.8
May	22.3	0.705	0.719	0.877	13.7	13.6	10.2	-2.6	-0.1	-1.1
June	24.7	0.698	0.705	0.855	14.3	14.0	11.1	-0.4	0.5	-0.7
July	26.2	0.716	0.693	0.877	15.7	15.8	11.4	-2.1	-0.2	-0.7
August	25.9	0.777	0.795	0.901	15.9	15.1	11.8	-1.8	-0.4	-1.0
September	31.5	0.741	0.795	0.901	18.5	15.8	12.6	-0.3	-0.4	-1.3
October	41.4	0.753	0.794	0.890	19.6	17.5	14.1	-2.9	0.0	-1.1
November	27.4	0.836	0.844	0.925	12.2	11.5	8.5	-2.2	-0.0	-0.6
December	40.1	0.826	0.836	0.925	15.5	14.4	10.4	-3.1	0.1	-0.7

Average	34.5	0.757	0.779	0.897	17.1	15.9	12.2	-2.5	-0.0	-1.0

As shown in the table, NO_2 observations peak during winter months. This is due to lower mixing heights and colder temperatures (leading to stronger NO_X emissions from e.g. heating and longer atmospheric lifetimes of NO_2). During the summer months, both scenarios A and B show the lowest RMSE, but also show poorer correlation. This can be explained the higher ratio of the RMSE to the mean observations of NO_2 during summer.

Note that the results for scenario A in March differ slightly from those in Table 3 (where for TROPOMI-only the city-wide correlation is 0.740, RMSE is 19.3 μg/m³, and bias is 0.8 μg/m³). This can be explained from the starting point of the processing (November 2018) being different from the main text (January 2019).

Additionally, in scenario A all months show negative biases, with the largest biases occurring in winter. This is likely due to the use of a fixed diurnal profile for residential emissions throughout the year (see Section S5). Introducing a seasonal component in this profile could improve the results.

S8 Monitoring stations in European cities

In Europe there are approximately 2800 cities with a population above 50,000. The European Environment Agency AirBase database (EEA, 2018) lists 2035 cities in 40 countries having at least 1 air quality monitoring station and 71 cities having at least 5 stations.

Table S2: Size of air quality monitoring network in European cities

Amount of reference stations	Number of cities
0	811
1	1571
2	245
3	104
4	44
5	26
6	17
7	4
8	7
9	6
10	2
11	3
12	1
13	2
15	1
17	1
25	1

Table S3: European cities having 5 or more reference stations

City	Country	Amount of reference stations
MADRID	Spain	25
WIEN	Austria	17
LONDON	United Kingdom	15
ROMA	Italy	13
AMSTERDAM	Netherlands	13
BERLIN	Germany	12
VALLADOLID	Spain	11
HAMBURG	Germany	11

SANTA CRUZ DE TENERIFE	Spain	11
ANTWERPEN	Belgium	10
BRUSSELS	Belgium	10
TARANTO	Italy	9
MILANO	Italy	9
ROTTERDAM	Netherlands	9
NAPOLI	Italy	9
PALERMO	Italy	9
PRAHA	Czech Republic	9
TRIESTE	Italy	8
CARTAGENA	Spain	8
BRINDISI	Italy	8
BARCELONA	Spain	8
ZARAGOZA	Spain	8
BUCHAREST	Romania	8
GENOVA	Italy	8
DUBLIN	Ireland	7
BELGRADE	Serbia	7
SAN ROQUE	Spain	7
SEVILLA	Spain	7
OSLO	Norway	6
HUELVA	Spain	6
VALENCIA	Spain	6
TORINO	Italy	6
STOCKHOLM	Sweden	6
LINZ	Austria	6
GRAZ	Austria	6
SIRACUSA	Italy	6
LA SPEZIA	Italy	6
Sofia	Bulgaria	6
PLZEN	Czech Republic	6
MARSEILLE	France	6
TOULOUSE	France	6
CAGLIARI	Italy	6
BARI	Italy	6
MANTOVA	Italy	6
LECCE	Italy	6
GUBBIO	Italy	5
MÁLAGA	Spain	5
SKOPJE	North Macedonia	5
ZÜRICH	Switzerland	5
UDINE	Italy	5
HELSINKI	Finland	5
DIJON	France	5
TARRAGONA	Spain	5
LE HAVRE	France	5

VENEZIA	Italy	5
SAINT-DENIS	France	5
NÍJAR	Spain	5
VICENZA	Italy	5
GDANSK	Poland	5
BUDAPEST	Hungary	5
GIJÓN	Spain	5
CASTELLÓN DE LA PLANA	Spain	5
PESCARA	Italy	5
CANDELARIA	Spain	5
BARRIOS (LOS)	Spain	5
CATANIA	Italy	5
GALATI	Romania	5
FERRARA	Italy	5
LISBOA	Portugal	5
WARSZAWA	Poland	5
TERNI	Italy	5

References

EPA: Technical support document (TSD) for NO2-related AERMOD modifications, U.S. Environmental Protection Agency, EPA-454/B-15-004, July 2015, 2015.

EEA, 2018. AirBase - the European Air quality dataBase, Version 8. European Environment Agency. https://www.eea.europa.eu/data-and-maps/data/airbase-the-european-air-quality-database-8, (Accessed November 27, 2018).

Guevara, M., Jorba, O., Tena, C., Denier van der Gon, H., Kuenen, J., Elguindi, N., Darras, S., Granier, C., and Pérez García-Pando, C.: Copernicus Atmosphere Monitoring Service TEMPOral profiles (CAMS-TEMPO): global and European emission temporal profile maps for atmospheric chemistry modelling, Earth Syst. Sci. Data, 13, 367–404, https://doi.org/10.5194/essd-13-367-2021, 2021.

Mijling, B.: High-resolution mapping of urban air quality with heterogeneous observations: a new methodology and its application to Amsterdam, Atmos. Meas. Tech., 13, 4601–4617, https://doi.org/10.5194/amt-13-4601-2020, 2020.